

THREE MODES OF METAL-ENRICHED STAR FORMATION IN THE EARLY UNIVERSE

BRITTON D. SMITH¹

525 Davey Laboratory, Department of Astronomy & Astrophysics, The Pennsylvania State University, University Park, PA 16802

MATTHEW J. TURK

Kavli Institute for Particle Astrophysics and Cosmology, 2575 Sand Hill Rd., Mail Stop 29, Menlo Park, CA 94025

STEINN SIGURDSSON

525 Davey Laboratory, Department of Astronomy & Astrophysics, The Pennsylvania State University, University Park, PA 16802

BRIAN W. O'SHEA²

Department of Physics & Astronomy, Michigan State University, East Lansing, MI 48824

AND

MICHAEL L. NORMAN

Center for Astrophysics and Space Sciences, University of California at San Diego, La Jolla, CA 92093

Draft version October 22, 2018

ABSTRACT

Simulations of the formation of Population III (Pop III) stars suggest that they were much more massive than the Pop II and Pop I stars observed today. This is due to the collapse dynamics of metal-free gas, which is regulated by the radiative cooling of molecular hydrogen. We study how the collapse of gas clouds is altered by the addition of metals to the star-forming environment by performing a series of simulations of pre-enriched star formation at various metallicities. To make a clean comparison to metal-free star formation, we use initial conditions identical to a Pop III star formation simulation, with low ionization and no external radiation other than the cosmic microwave background (CMB). For metallicities below the critical metallicity, Z_{cr} , collapse proceeds similarly to the metal-free case, and only massive objects form. For metallicities well above Z_{cr} , efficient cooling rapidly lowers the gas temperature to the temperature of the CMB. The gas is unable to radiatively cool below the CMB temperature, and becomes thermally stable. For high metallicities, $Z \gtrsim 10^{-2.5} Z_{\odot}$, this occurs early in the evolution of the gas cloud, when the density is still relatively low. The resulting cloud-cores show little or no fragmentation, and would most likely form massive stars. If the metallicity is not vastly above Z_{cr} , the cloud cools efficiently but does not reach the CMB temperature, and fragmentation into multiple objects occurs. We conclude that there were three distinct modes of star formation at high redshift ($z \gtrsim 4$): a ‘primordial’ mode, producing massive stars (10s to 100s M_{\odot}) at very low metallicities ($Z \lesssim 10^{-3.75} Z_{\odot}$); a CMB-regulated mode, producing moderate mass (10s of M_{\odot}) stars at high metallicities ($Z \gtrsim 10^{-2.5} Z_{\odot}$ at redshift $z \sim 15-20$); and a low-mass (a few M_{\odot}) mode existing between those two metallicities. As the universe ages and the CMB temperature decreases, the range of the low mass mode extends to higher metallicities, eventually becoming the only mode of star formation.

Subject headings: stars: formation, cosmology

1. INTRODUCTION

Understanding the nature of the first stars in the universe is, in principle, a very straightforward problem to solve. The initial conditions are defined by well-constrained cosmological parameters (e.g., Spergel et al. (2007); Komatsu et al. (2008)) and accepted calculations of Big Bang Nucleosynthesis (e.g., Smith et al.

(1993)). The relative simplicity of the chemistry of primordial gas (Abel et al. 1997; Galli & Palla 1998), along with powerful numerical methods, have made it possible to accurately characterize the formation process of primordial stars from the assembly of their dark matter halos through the end of the optically-thin regime of the collapsing protostar (Abel et al. 2002; Bromm et al. 2002; Bromm & Loeb 2004; Yoshida et al. 2006; O’Shea & Norman 2007; Gao et al. 2007). Results from theory and numerical simulations suggest that the first stars were 10s to 100s M_{\odot} (Abel et al. 2002; Omukai & Palla 2003; Tan & McKee 2004; Yoshida et al. 2006; O’Shea & Norman 2007). A direct calculation, however, involves simulating the complex processes of accretion and radiative feedback, a capability currently just beyond the state of the art. In

Electronic address: brittons@origins.colorado.edu
Electronic address: mturk@slac.stanford.edu
Electronic address: steinn@astro.psu.edu
Electronic address: oshea@msu.edu
Electronic address: mlnorman@ucsd.edu

¹ Center for Astrophysics & Space Astronomy, Department of Astrophysical & Planetary Sciences, University of Colorado, Boulder, CO, 80309

² Theoretical Astrophysics Group, Los Alamos National Laboratory, Los Alamos, NM 87545

contrast, the challenge of understanding the second generation of stars is significantly more complex. The initial conditions of the first stars essentially depend only on the principles of cold dark matter cosmology and the properties of molecular hydrogen, but the initial conditions of the second stars require a complete solution to the formation and evolution of their predecessors as well as host of additional chemistry and physical processes. The chemical composition and physical conditions of second-generation star-forming environments strongly depend on the exact masses of the first stars (Heger & Woosley 2002; Maeder et al. 2005; Nomoto et al. 2006; Rockefeller et al. 2006) and the mechanics of their supernovae (Kitayama & Yoshida 2005; Greif et al. 2007).

At the heart of the problem regarding forming the second stars is understanding how the star formation process is altered by the introduction of the first metals in the universe, created in the explosions of the first stars. The chemical composition of a gas determines the efficiency with which it can cool radiatively. Cold, metal-free gas ($T < 10^4$ K) cools solely through ro-vibrational lines of H_2 , whose lowest-lying transition has an energy equivalent temperature of ~ 512 K, resulting in a minimum achievable temperature of ~ 200 K. The energy levels of H_2 become thermalized at rather low densities, $n \sim 10^{3-4} \text{ cm}^{-3}$, where n is the number density, above which the cooling rate is only proportional to n , instead of n^2 . Numerical simulations have shown that this creates a stalling point in the star formation process, where the free-fall collapse of metal-free gas comes to a halt as the cooling time increases to be significantly above the dynamical time (Abel et al. 2002; Bromm et al. 2002). Entry into this ‘loitering’ phase marks the end of hierarchical fragmentation that occurs during the free-fall period, a fragmentation that occurs because the temperature is able to continually decrease with increasing density. The final fragmentation mass scale is then set by the Jeans mass at the temperature and density corresponding to the point where the gas can no longer get colder with increasing density (Larson 1985, 2005). In the metal-free case, this yields a mass scale of $\sim 1000 M_\odot$, resulting in the high-mass nature of the first stars.

The addition of metals enhances the cooling rate at low temperatures through fine-structure and molecular transitions, as well as by continuum emission from dust grains. At low to moderate densities ($n < 10^9 \text{ cm}^{-3}$), only metals in the gas phase contribute significantly to the cooling, unless the level of metal enrichment is very high (Smith et al. 2008). In the phases where H_2 cooling is strong ($n \lesssim 10^4 \text{ cm}^{-3}$, an increase in the cooling due to metals is first seen only at temperatures less than the 200 K temperature minimum that exists in metal-free star formation (Smith et al. 2008). At abundances of $Z \lesssim 10^{-4} Z_\odot$, where metal cooling is only significant for $T < 200$ K, the low-density evolution of the cloud is identical to the metal-free case (Omukai 2000; Bromm et al. 2001; Omukai et al. 2005). At higher metallicities, gas-phase metal cooling becomes strong enough for the collapsing cloud to bypass the loitering phase and to undergo continued fragmentation (Bromm et al. 2001; Bromm & Loeb 2003; Santoro & Shull 2006; Smith & Sigurdsson 2007). If dust grains are present, their influence becomes im-

portant at very high densities ($n > 10^{12} \text{ cm}^{-3}$). This has been shown to induce fragmentation for metallicities as low as $10^{-5.5} Z_\odot$ (Omukai et al. 2005; Schneider et al. 2006; Tsuribe & Omukai 2006; Clark et al. 2008). Calculations by Schneider et al. (2004) predict that up to 30% of the progenitor mass is converted into dust in a pair-instability supernova, but observations of Type II supernova in the local universe remnants have not returned conclusive evidence of dust (Green et al. 2004; Krause et al. 2004). In the context of star formation in the early universe, the arrival at this critical metallicity, Z_{cr} , at which fragmentation occurs beyond the capabilities of primordial gas, is predicted to be the point where the universal mode of star formation shifts permanently from the high-mass, solitary mode of the first stars, to the low-mass, multiply-producing mode that is presently observed (Bromm & Loeb 2003; Santoro & Shull 2006; Smith & Sigurdsson 2007).

The protostellar collapse of metal-enriched gas clouds has been studied extensively with one-zone models coupled to large chemical networks (Omukai 2000; Schneider et al. 2003; Omukai et al. 2005; Schneider et al. 2006). These studies have produced insight into the evolution of the density and temperature of collapsing gas clouds with finite metallicities, but one-zone models cannot speak to the actual process of fragmentation, which requires attention to complex cloud geometries that can only be given by fully three-dimensional hydrodynamic simulations (Larson 2007). The first of such simulations were carried out by Bromm et al. (2001), who included cooling from C, N, O, Fe, S, and Si, but not H_2 , finding that clouds with metallicities, $Z \geq 10^{-3} Z_\odot$ are able to fragment to mass scales lower than in the metal-free case. These simulations had a mass resolution of only $100 M_\odot$ and were, therefore, unable to investigate the formation of solar-mass stars. More recently, Smith & Sigurdsson (2007) have performed a series of high-resolution simulations of metal-enriched gas collapse that were able to follow the evolution of gas fragments to sub-solar mass scales. They, too, find that gas with metallicities, $Z \geq 10^{-3} Z_\odot$ will fragment into multiple clumps, while gas with $Z \leq 10^{-4} Z_\odot$ will produce only one object. However, Smith et al. (2008) reported the existence of regions in density and temperature that are thermally unstable in gas with metallicities as low as $10^{-4} Z_\odot$. Fragmentation is traditionally thought to happen when the cooling time is less than the dynamical time, as the gas is able to cool and form perturbations before they can be smoothed out by sound waves. When this condition, referred to as the fragmentation criterion, is satisfied, fragmentation can also be aided by thermal instabilities (Field 1965), where a slight decrease in temperature or increase in density leads to a higher cooling rate, causing differences in temperature between pockets of gas to grow in a runaway fashion. In the adaptive mesh refinement simulations of Smith & Sigurdsson (2007), grid refinement was performed based on baryon and dark matter overdensities and by ensuring that the Truelove criterion, $l_J < \Delta x$, where l_J is the local Jeans length and Δx is the grid cell size, was satisfied (Truelove et al. 1997). However, refinement was not performed when the cooling time was less than the hydrodynamic time-step. While this was not explicitly

TABLE 1
SIMULATIONS

Run	IC	$Z (Z_{\odot})$	z_{col}	Grids	Cells ($\times 10^7$)	n_{max} (cm^{-3})	Δt_{col} (yr)
r1_mf	1	0	14.761	13790	6.49	5.96×10^{11}	-
r1_Z-6	1	10^{-6}	14.762	13015	6.42	6.43×10^{11}	2.9×10^4
r1_Z-5	1	10^{-5}	14.783	12889	6.43	6.74×10^{11}	5.7×10^5
r1_Z-4.25	1	$10^{-4.25}$	14.809	12955	6.40	6.75×10^{11}	1.2×10^6
r1_Z-4	1	10^{-4}	14.830	12964	6.38	6.22×10^{11}	1.8×10^6
r1_Z-3.75	1	$10^{-3.75}$	14.848	13003	6.38	6.97×10^{11}	2.2×10^6
r1_Z-3.5	1	$10^{-3.5}$	14.874	12883	6.40	6.89×10^{11}	2.9×10^6
r1_Z-3.25	1	$10^{-3.25}$	14.936	12888	6.36	3.97×10^{11}	4.5×10^4
r1_Z-3	1	10^{-3}	15.073	12581	6.25	4.42×10^{11}	7.9×10^6
r1_Z-2.5	1	$10^{-2.5}$	16.180	11187	5.69	4.70×10^{11}	3.3×10^7
r1_Z-2	1	10^{-2}	19.481	8693	4.57	1.56×10^{11}	8.8×10^7
r2_mf	2	0	17.409	8684	4.76	7.97×10^{11}	-
r2_Z-4	2	10^{-4}	17.555	8509	4.74	8.39×10^{11}	2.5×10^6
r2_Z-3.5	2	$10^{-3.5}$	17.654	8476	4.71	8.20×10^{11}	4.2×10^6
r2_Z-3	2	10^{-3}	17.955	8408	4.67	7.30×10^{11}	9.2×10^6
r2_Z-2.5	2	$10^{-2.5}$	18.537	8022	4.51	4.41×10^{11}	1.8×10^7
r2_Z-2	2	10^{-2}	20.441	7194	4.09	1.92×10^{11}	4.4×10^7
r3_mf	3	0	23.885	7771	4.25	1.63×10^{12}	-
r3_Z-4	3	10^{-4}	23.966	7722	4.23	1.65×10^{12}	6.7×10^5
r3_Z-3.5	3	$10^{-3.5}$	24.122	7640	4.21	1.42×10^{12}	1.9×10^6
r3_Z-3	3	10^{-3}	24.390	7366	4.17	1.29×10^{12}	4.1×10^6
r3_Z-2.5	3	$10^{-2.5}$	24.732	7145	4.13	1.20×10^{12}	6.7×10^6
r3_Z-2	3	10^{-2}	25.028	7083	4.09	6.53×10^{11}	8.9×10^6
r3_Z-2noCMB	3	10^{-2}	25.255	7424	4.29	6.02×10^{11}	1.1×10^7

NOTE. — z_{col} is the redshift at the onset of runaway collapse. The total number of grid cells includes those that are covered by child grids at higher levels of refinement. n_{max} is the proper maximum baryon number density within the box. Δt_{col} is the time difference to runaway collapse from the metal-free case.

wrong, since the radiative cooling solver iterates with time-steps that are no larger than 10% of the cooling time, it may have artificially suppressed the growth of thermal instabilities that could have formed extra fragments.

We rerun the simulations of Smith & Sigurdsson (2007) with an additional refinement criterion which ensures that the hydrodynamic time-step is always less than the cooling time on the finest level of resolution. In addition, we extend the series of simulations to include lower metallicities and to more carefully examine the metallicity range between $10^{-4} Z_{\odot}$ and $10^{-3} Z_{\odot}$. We also run similar simulations with two extra sets of initial conditions to confirm the robustness of the results. We describe the setup of our simulations and the improvements over Smith & Sigurdsson (2007) in §2. In §3, we calculate the gas-phase critical metallicity, evaluate the validity of our assumption of optical thinness, and present the results of the suite of simulations. In §4, we discuss our results in the context of star formation at high redshift and make the case for an initial mass function (IMF) that evolves over cosmic time. We also include a discussion of the caveats and limitations of this work. Finally, we conclude with a brief summary of the main conclusions of this work in §5.

2. SIMULATION SETUP

We perform a series of 24 primordial star formation simulations using the Eulerian adaptive mesh refinement hydrodynamics + N-body code, Enzo (Bryan & Norman 1997; O’Shea et al. 2004). Excluding our three metal-free control runs, the gas in each simulation is homogeneously pre-enriched to some non-zero metallicity. As in

Smith & Sigurdsson (2007), we confine the simulations to constant metallicities with solar abundance patterns, saving the more realistic, and far more complicated, simulations of true second-generation star-forming environments, with heterogeneous metal-mixing and nonsolar abundance patterns, for a future work.

The nature of the initial conditions for our simulations are identical to those used in Smith & Sigurdsson (2007). The simulation box has a comoving size of $300 h^{-1}$ kpc, with 128^3 grid cells on the top grid and three nested sub-grids, each refining by a factor of 2, for an effective top grid resolution of 1024^3 cells. The cosmological parameters have the following values: $\Omega_M = 0.3$, $\Omega_{\Lambda} = 0.7$, $\Omega_B = 0.04$, and Hubble constant, $h = 0.7$, in units of $100 \text{ km s}^{-1} \text{ Mpc}^{-1}$. The power spectrum of initial density fluctuations is given by Eisenstein & Hu (1999), with $\sigma_8 = 0.9$ and $n = 1$. Refined grids are created during the simulations when the baryon (dark matter) density is 4 (8) times greater than the mean density at that level. The density threshold for refinement decreases at higher levels. The local Jeans length is resolved by a minimum of 16 grid cells at all times, exceeding the Truelove criterion (Truelove et al. 1997) by a factor of four along each coordinate axis. In addition, grid refinement occurs whenever the cooling time drops below the integration time step of the hydrodynamic solver. This final refinement criterion was not used in Smith & Sigurdsson (2007). During the simulation, a grid cell is flagged for refinement if one or more of any of these criteria are met.

We perform three sets of simulations. Qualitatively, the three sets are the same. They each have the same cosmological parameters, box size, and resolution. The only difference between them is that their initial condi-

tions were created with three unique randomizations of the initial density and velocity perturbations. Thus, they represent three different realizations of the same problem. The first set of initial conditions is the one used by Smith & Sigurdsson (2007). The second and third sets were initially used by O’Shea & Norman (2007) and correspond to the runs named L0_30A and L0_30D in that work. For each set of initial conditions, we perform a metal-free control run. Excluding the control runs, we run 10 simulations using initial conditions Set 1, with metallicities ranging from $10^{-6}Z_{\odot}$ to $10^{-2}Z_{\odot}$, 5 simulations using Set 2, and 6 simulations using Set 3, with metallicities from $10^{-4}Z_{\odot}$ to $10^{-2}Z_{\odot}$ for Sets 2 and 3. The final simulation in Set 3 has a metallicity of $10^{-2}Z_{\odot}$, but unlike the others, excludes the effect of the CMB on the cooling of gas.

We use the second implementation of the optically-thin metal cooling method of Smith et al. (2008). This method uses tabulated cooling functions created with the photoionization software, Cloudy (Ferland et al. 1998), for all elements heavier than He, up to atomic number 30 (Zn). A solar abundance pattern is used for the metals in all of the simulations. Since we only follow the evolution of the collapsing clouds up to densities of $\sim 10^{12} \text{ cm}^{-3}$, we neglect the cooling from dust and assume the presence of only gas-phase metals. In §3.3, we calculate the optical depth in the collapsing cloud for the most important high density, gas-phase metal coolants and find that the optically thin assumption holds at all times during simulations. The H/He chemistry is followed explicitly during the simulation as in Abel et al. (1997) and Anninos et al. (1997), but including reactions that extend its validity to above 10^8 cm^{-3} . See Smith et al. (2008) for a full discussion of this method. We neglect cooling from HD, as Bromm et al. (2002) found its contribution to be negligible in situations where the initial ionization is low, such as in this work. However, it has been pointed out by Glover (2008) that when the initial ionization is high, the HD fraction can become enhanced to the point where HD cooling is important. Heating from H_2 formation is not included in the chemical network. This may contribute a significant source of heat when H_2 formation via three-body reactions becomes important at $n \gtrsim 10^9 \text{ cm}^{-3}$ (Omukai et al. 2005). However, we argue in §3.4 that our results are robust despite this shortcoming. The metal cooling data was created with the Linux computer cluster Lion-xo which is operated by the High Performance Computing Group at The Pennsylvania State University.

As in the precursor to this work (Smith & Sigurdsson 2007), we do not assume the existence of an ionizing UV background. The Population III stars responsible for the enrichment of the gas in our simulations have died, and we assume any living Pop III stars are most likely too distant to contribute significant amounts of radiation. A major difference between our simulations and those of Smith & Sigurdsson (2007) is the choice of H_2 cooling rates. We use the updated H_2 cooling rates of Galli & Palla (1998), whereas Smith & Sigurdsson (2007) used the older rates of Lepp & Shull (1984). The rates of Galli & Palla (1998) are generally lower than those of Lepp & Shull (1984), causing the gas to take longer to cool in the newer simulations. As a result, the moment of runaway-collapse in our simulations is sys-

tematically delayed from those of Smith & Sigurdsson (2007), when comparing the simulations in Set 1.

Each simulation is initialized at $z = 99$ and runs until the point where at least one dense, prestellar core forms within a $\sim 5 \times 10^5 M_{\odot}$ dark matter halo, located in the center of the simulation box. The simulations are stopped when a maximum refinement of 24 levels below the top grid has been reached. This corresponds to a maximum density of $\sim 10^{11} \text{ cm}^{-3}$, or roughly $3 \times 10^{-13} \text{ g cm}^{-3}$. The simulations were run on DataStar, an IBM Power4 machine at the San Diego Supercomputing Center. A summary of the final state of each simulation is given in Table 1.

3. RESULTS

3.1. Critical Metallicities

The gas phase critical metallicity, Z_{cr} , has been estimated analytically by calculating the chemical abundance required for the cooling time to equal the dynamical time at the stalling point for metal-free gas, $n \sim 10^{3-4} \text{ cm}^{-3}$ and $T \sim 200 \text{ K}$. Bromm & Loeb (2003) performed this exercise with C and O, but excluding cooling from H_2 , and Santoro & Shull (2006) did so with C, O, Fe, Si, and including H_2 . Santoro & Shull (2006) considered densities above and below the stalling point as well. The general consensus from these studies is that $Z_{cr} \approx 10^{-3.5} Z_{\odot}$ at $n = 10^4 \text{ cm}^{-3}$.

We observe a small amount of variance in the values of the density and temperature at which the temperature minimum occurs in our three metal-free runs. Since the exact value of the critical metallicity depends on the precise conditions at the temperature minimum, i.e., temperature, total density, and H_2 density, we calculate the critical metallicity for each of the three runs separately. To do this, we define the cooling time in the following way:

$$t_{cool} = \frac{nkT}{(\gamma - 1)[\Lambda'_{\text{H}_2} + \Lambda'_{\text{metals}}]}, \quad (1)$$

where k is Boltzmann’s constant, γ is $5/3$, and Λ'_{H_2} and Λ'_{metals} are the cooling rates from H_2 and the metals in units of $[\text{erg s}^{-1} \text{ cm}^{-3}]$. We use Λ' to avoid confusion with the term, Λ , which is often expressed in units of $[\text{erg s}^{-1} \text{ cm}^3]$. We then set Equation 1 equal to the dynamical time,

$$t_{dyn} = \sqrt{\frac{3\pi}{16G\rho}}, \quad (2)$$

where G is the gravitational constant and ρ is the mass density. We calculate Z_{cr} for the conditions at the temperature minimum in each metal-free simulation using the H_2 cooling rates of Galli & Palla (1998) and the metal cooling rates from Smith et al. (2008). The results are shown in Table 2. The systematic shift toward lower values of Z_{cr} compared to previous calculations is most likely due to the fact that the minimum temperatures are slightly higher than 200 K, where both the H_2 and metal cooling rates are higher. In addition, cooling from H_2 was not included in the calculation of Bromm & Loeb (2003), meaning that more cooling from the metals would have been required. There is a correlation between Z_{cr} and the collapse redshift of the simulation, with the highest value of Z_{cr} coming from the highest collapse redshift, despite the lack of such a correlation for n , n_{H_2} , or T . However,

TABLE 2
CRITICAL METALLICITIES

Run	n [cm $^{-3}$]	n_{H_2} [cm $^{-3}$]	T	$\log(Z_{cr}/Z_{\odot})$
r1_mf	6.89×10^3	3.42	283	-4.08
r2_mf	3.64×10^3	1.86	214	-3.90
r3_mf	1.19×10^4	6.53	260	-3.85

NOTE. — Critical metallicities calculated for each metal-free simulation. n , n_{H_2} , and T are the proper number density, H_2 number density, and temperature at the temperature minimum where H_2 becomes thermalized in each of the metal-free simulations. The final column is the log of the metallicity required to equate the cooling time to the dynamical time for the conditions listed.

there is a correlation between the H_2 fraction and collapse redshift, which has been observed in the Pop III simulations of O’Shea & Norman (2007). They find that the higher H_2 fractions result from the generally warmer gas in halos that collapse at higher redshifts, which is simply a function of the linear dependence upon redshift of the virial temperature. This may be the dominant factor, but with only 3 data points it is unclear whether the observed trend is even significant. In addition, the artificial nature of our initial conditions may make this finding inapplicable to the real world.

We see a trend with metallicity and collapse redshift that is similar to what was reported by Smith & Sigurdsson (2007), where simulations with higher metallicities reach the runaway collapse phase earlier. We define Δt_{col} as the difference in time to runaway collapse between a simulation with non-zero metallicity and the metal-free run with the same initial conditions. An increase in metallicity by 0.5 dex results in an increase in Δt_{col} by a factor of approximately 1.3 to 4. Similarly, when compared within a set, the simulations collapsing later have a higher number of total grids and grid cells in their final output, since the lower-density envelope gas has had more time to evolve and reach higher densities.

3.2. Radial Profiles

In Figure 1, we show projections of mass-weighted mean number density for the central 0.5 pc surrounding the point of maximum baryon density for the final output of all runs in Set 1. For the runs with metallicities near or below Z_{cr} ($10^{-4.08} Z_{\odot}$ for this set of simulations), the central cores appear quite round and show no clear signs of forming more than one object. In the metallicity range from $10^{-3.75} Z_{\odot}$ to $10^{-3.25} Z_{\odot}$, the cores appear increasingly asymmetric, with at least one additional density maximum present. However, at metallicities at or above $10^{-3} Z_{\odot}$, the cores return to a more spherical shape with only a single density maximum.

In Figure 2, we plot spherically averaged, mass-weighted values of the density, temperature, enclosed mass, and radial velocity as a function of radius from the point of maximum density for all simulations in Set 1. On large scales, the density profiles follow an $r^{-2.2}$ power law. To highlight the difference in density between each run, we plot in panel A of Figure 2 the value of $(n \times r^2)$, instead of simply n . We choose to scale the density by r^2 instead of $r^{2.2}$ because it is easier to glean the true density from the figure. Over most of the plot-

ted range, the run with the lowest metallicity has the highest density. In the isothermal collapse model of Shu (1977), the accretion rate is proportional to the cube of the sound speed, or $T^{3/2}$. Figure 2B shows that while isothermality does not really apply, there is a clear correlation between the temperature and density. The runs with the highest metallicity, and subsequently the coldest gas, are the least dense. In addition, within individual runs, an increase in the gas temperature is matched by an increase in the density.

The instantaneous accretion rate at a given radius is a function of the infall velocity at that position. Although there are some exceptions, the correlation between temperature/sound speed and infall velocity, with higher temperatures/sound speeds corresponding to higher velocities, generally holds. This was also found to be true by O’Shea & Norman (2007) in their simulations of Pop III star formation. We find that the inflow is roughly transonic throughout the entire density range, showing that even though the collapsing clouds are not isothermal spheres, their accretion rates are still largely regulated by the sound speed.

3.3. Optical Depth

The fragmentation of collapsing gas depends sensitively on its thermal evolution, which is effectively a measure of the radiative cooling properties of the gas as a function of density and temperature. Since our radiative cooling method, described above, assumes optical thinness, the results of our simulations are only valid where $\tau \ll 1$. The optically thin assumption begins to break down at densities $n \gtrsim 10^{10}$ cm $^{-3}$ (Omukai et al. 2005). The optical depth at a frequency ν is expressed as

$$\tau_{\nu} = \int \kappa_{\nu} \rho dl, \quad (3)$$

where κ_{ν} is the opacity, ρ is the mass density, and dl is the distance traveled by a photon. At a given density, the cloud has a characteristic size $r(\rho)$, shown in Figure 2A. If a photon emitted from a region with density ρ is able to travel a distance $\sim r(\rho)$ without being re-absorbed, then it will not alter the thermal evolution of the cloud, and the assumption of optical thinness holds. Using the Cloudy software, we calculate values of the absorption coefficient, $\alpha_{\nu} \equiv \kappa_{\nu} \rho$, as a function of density, metallicity, temperature, and frequency. Equation 3 then takes the form

$$\tau_{\nu} = \alpha_{\nu}(\rho, Z, T) r(\rho). \quad (4)$$

For metallicities $Z \lesssim 10^{-2} Z_{\odot}$ and in the absence of dust, metal cooling is dominated by fine-structure transitions of OI and FeII (Santoro & Shull 2006; Smith et al. 2008). In Figure 3, we plot the optical depth from Equation 4 for the FeII line at 25.99 μm and the OI line at 63.18 μm as a function of density using the spherically-averaged densities and temperatures shown in Figure 2. At low energies and in the absence of dust grains, the largest contributor to the opacity is free-free absorption, which is dominated by H for low metallicities. As a result, the opacity in the energy range of interest is essentially independent of metallicity for metallicities less than solar. When the metals become a considerable fraction of the total gas content, above $Z \sim 10 Z_{\odot}$ or so, the opacity at

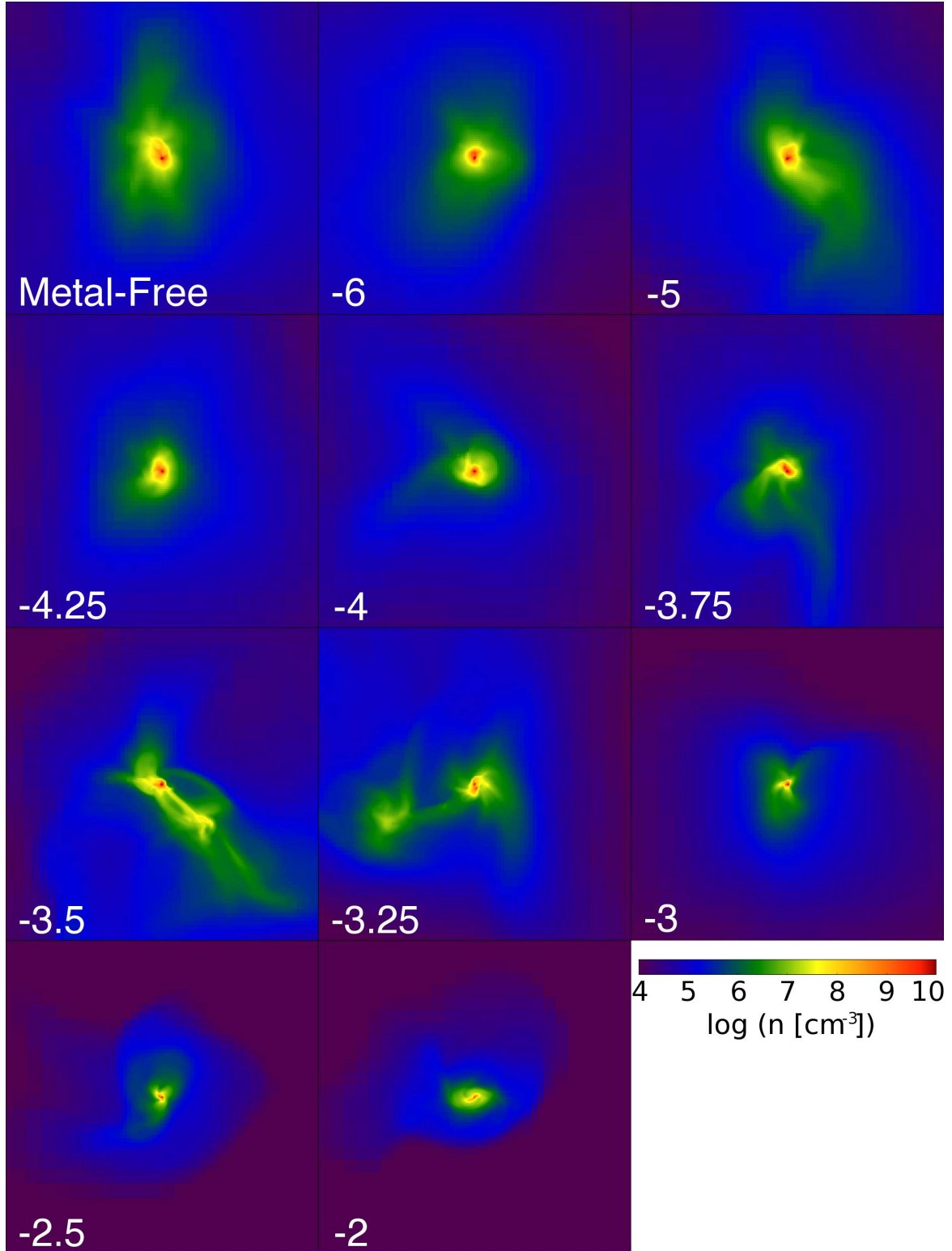


FIG. 1.— Projections of mass-weighted mean number density for the final output of all runs in Set 1. Each projection is centered on the location of maximum density in the simulation box and has a width of 0.5 pc proper. The labels in each panel indicate the log of the metallicity with respect to solar for that run. The images were made with the YT analysis toolkit (Turk 2008, yt.enzo-tools.org).

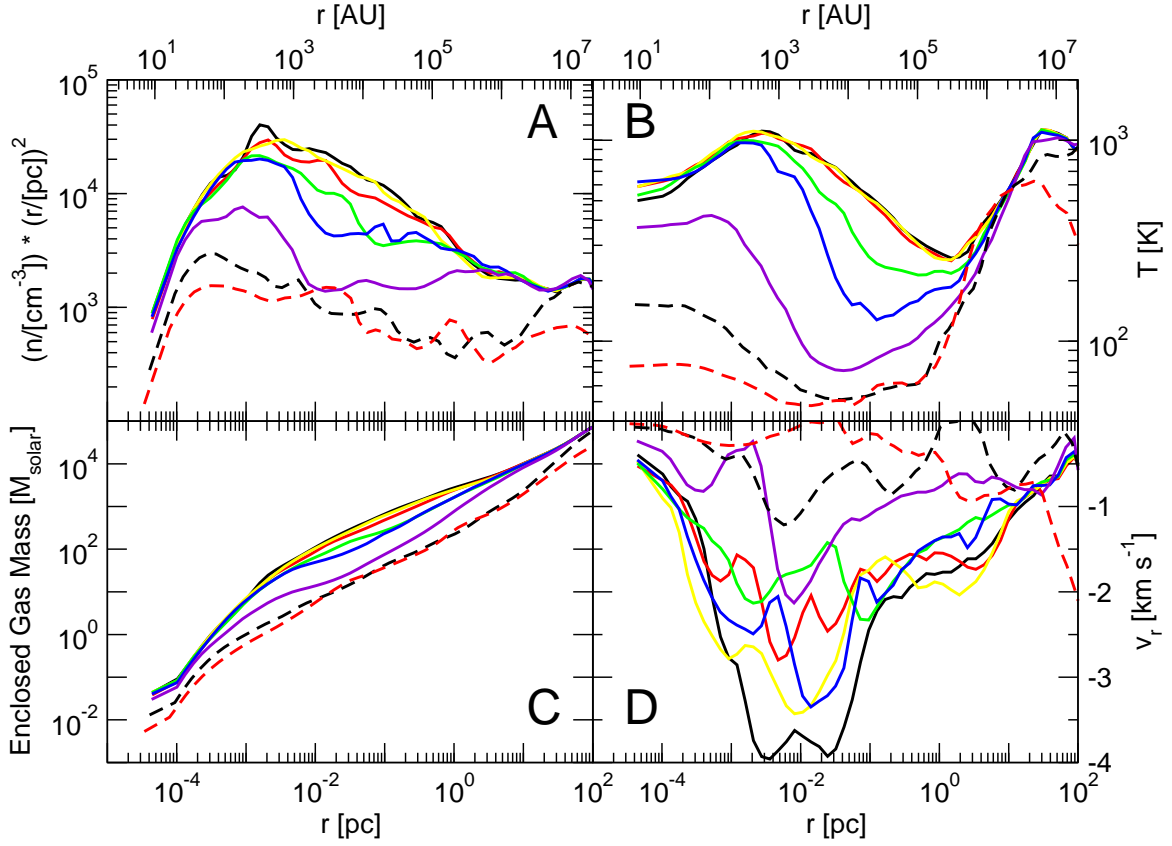


FIG. 2.— Spherically-averaged, mass-weighted quantities as a function of radius from the point of maximum density for 7 of the 10 simulations in Set 1. A: number density normalized to an r^{-2} power law; B: temperature; C: enclosed gas mass; D: radial velocity. In each panel, the metallicities are $Z = 0$ (solid-black), $10^{-6}Z_{\odot}$ (solid-red), $10^{-5}Z_{\odot}$ (yellow), $10^{-4}Z_{\odot}$ (green), $10^{-3.5}Z_{\odot}$ (blue), $10^{-3}Z_{\odot}$ (purple), $10^{-2.5}Z_{\odot}$ (dashed-black), and $10^{-2}Z_{\odot}$ (dashed-red).

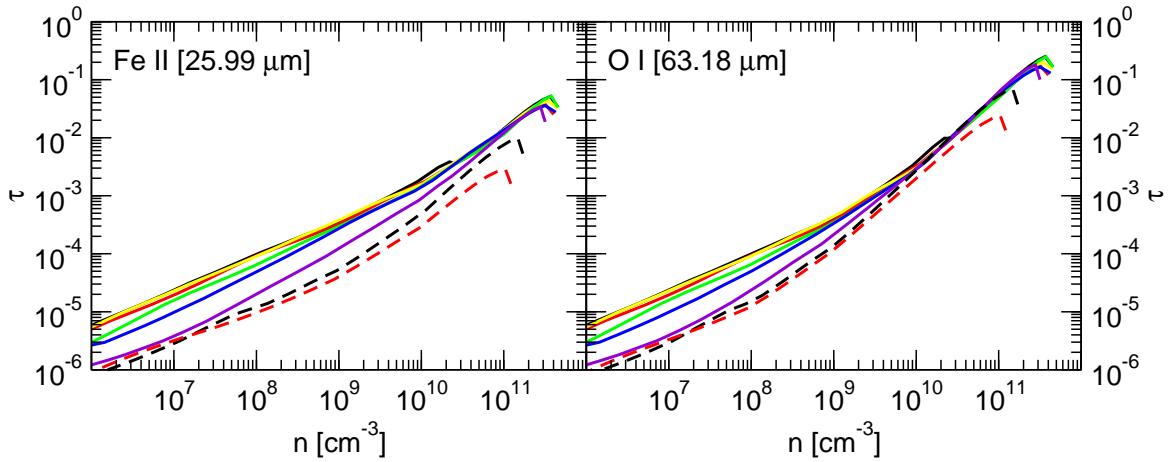


FIG. 3.— Optical depth for two of the most important high density, gas-phase coolants, FeII [25.99 μm] (left) and OI [63.18 μm] (right), as a function of density for runs in Set 1. The colors are the same as in Figure 2.

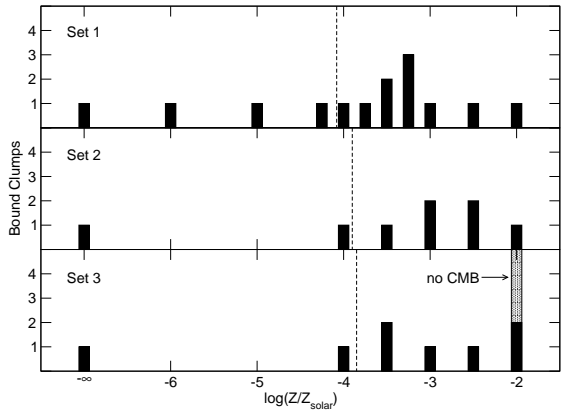


FIG. 4.— The number of bound clumps found within a sphere of radius 5 pc, centered on the point of maximum density, as a function of metallicity for all of the simulations performed. The grey bar in the bottom panel denotes the run where the temperature floor created by the CMB was not included. In each panel, the vertical dashed line represents the estimated value of Z_{cr} for each set from Table 2.

low energy for dust-free gas begins to grow with metallicity. In Figure 3, the apparent decrease in the optical depth at the highest metallicities is due to the flattening of the density profile at small radii. As such, the final point for each curve in Figure 3 should be ignored. For values inside the point where the density profile flattens, it would be more reasonable to use the radius at which the density turns over for the calculation of τ . Fortunately, τ remains significantly less than 1 throughout all of our simulations, peaking at roughly 0.25 at the highest densities for the runs with the lowest metallicities. The lower optical depth in the higher metallicity runs is due to the smaller characteristic size of the core, as seen in Figure 2A. It should also be noted that some molecules are missing from the Cloudy dust-free chemistry network that could contribute to the opacity, such as TiO. As such, the optical depths calculated could be slightly higher for the high metallicity simulations. However, we show in §3.4 that fragmentation in our simulations occurs well before this becomes a concern.

3.4. Fragmentation

In order to quantify the degree of fragmentation within each run, we employ a clump finding algorithm to search for bound clumps within 5 pc of the density maximum. As in Truelove et al. (1998), we define a clump, there referred to as a fragment, as “the mass contained between a local density maximum and the lowest isodensity surface surrounding only that maximum,” to quote that work. We begin by identifying all grid cells within a sphere of radius 5 pc, centered on the point of maximum density. We then create density contours using all the cells within the sphere. In density space, the first contour spans the entire range of density within the sphere, effectively creating one large contour. The contour becomes the parent clump of all other clumps that will be found as the process continues. On the second iteration, we create contours with the same maximum as before, but with the minimum increased by 1/4 dex. If more than one contour exists, those groups of cells become child clumps of the group made by the previous iteration. The process continues in a recursive fashion, creating groups of cells based on contours of increasing minimum density,

TABLE 3
FRAGMENTATION PROPERTIES

Run	Clump Mass [M_{\odot}]	n_{frag} [cm^{-3}]
r1_Z-3.5	54.4, 4.98	1.55×10^7
r1_Z-3.25	22.1	1.55×10^6
	5.46, 1.40	8.73×10^6
r2_Z-3	6.26, 1.89	2.75×10^9
r2_Z-2.5	95.6, 27.7	2.76×10^4
r3_Z-3.5	54.4, 4.98	1.55×10^5
r3_Z-2	289, 105	1.55×10^4
r3_Z-2noCMB	11.7	2.76×10^4
	4.38, 4.06	4.91×10^5
	32.6, 0.49	8.73×10^5

NOTE. — Number density at which fragmentation occurs within simulations where multiple bound clumps are identified and the masses of the clumps associated with that episode of fragmentation. The fragmentation density is taken to be the minimum density within a clump, taken from the earliest data output where that clump is identified.

identified only within the cells of the parent clump. The clump finding ends when minimum countour density has reached the constant maximum. Effectively, we create a family tree of clumps, with the very first group as the trunk of the tree. During the clump finding process, a child clump is only kept if it is gravitationally self-bound, or has children of its own that are bound. When determining whether a clump is bound, we consider the thermal energy of the gas as well its kinetic energy with respect to the bulk center of motion.

In Figure 4, we plot a histogram of all the number of clumps found in each run within the 5 pc sphere, as a function of the metallicity of the run. For this plot, we only include bound child clumps with no children of their own. When enlarging the radius of the sphere from 5 pc to 10 pc, no additional clumps were found in any of the runs. Figure 4 confirms what is seen in Figure 1. In all runs with metallicities below Z_{cr} , only a single bound clump is found. As the metallicity increases, the number of clumps increases, then decreases back to only a single clump for the highest metallicities, with the exception of r3_Z-2, which has 2 bound clumps. The range of metallicities where fragmentation occurs is consistent between Sets 1 and 3, but offset by 0.5 dex toward higher metallicities for Set 2. It is not clear what causes this offset, but the qualitative trend of increasing and then decreasing number of clumps exists in all 3 sets. It is also worthwhile to note that runs r1_Z-4, r1_Z-3.75, and r2_Z-3.5, while slightly above Z_{cr} , do not show fragmentation.

During the simulations, the Enzo code creates a snapshot of the entire box each time the maximum level of refinement increases. This provides us with multiple data outputs as the central density increases during runaway collapse. We ran the clump finder on all data outputs created during this period, searching for the first data output in which multiple clumps are found. Within this output, we take the minimum density within the clump to be the density at which fragmentation occurred. In Table 3, we list the fragmentation densities for all simulations in which multiple clumps were found. In runs with 2 clumps, the fragmentation density is the same for both clumps, since it represents the lowest density contour for which the two objects are separate. In run

r1_Z-3.25, which has 3 clumps, the core initially fragmented into 2 clumps at $n = 1.55 \times 10^6 \text{ cm}^{-3}$. One data output later, one of those clumps fragmented again at $n = 8.73 \times 10^6 \text{ cm}^{-3}$. A similar thing occurred in run r3_Z-2noCMB with 4 clumps forming initially and one of those fragmenting again later.

At densities of roughly 10^9 cm^{-3} , H_2 formation via three-body reactions begin to rapidly increase the H_2 fraction (Abel et al. 2002; Bromm et al. 2002). In our simulations, we find the H_2 fraction to be roughly constant at $\sim 10^{-3}$ until the density reaches $\sim 10^9 \text{ cm}^{-3}$. At densities of a few $\times 10^{10} \text{ cm}^{-3}$, the H_2 fraction has passed 10% and continues to rise. The onset of rapid H_2 formation occurs slightly earlier (within a factor of a few in density) in the runs with higher metallicity due to the T^{-1} dependence of the three-body rate coefficients. Our chemical network lacks heating from H_2 formation ($\sim 4.4 \text{ eV}$ per reaction), which may significantly raise the temperature of the gas when three-body reactions become important (Omukai et al. 2005). We test this by calculating the ratio of the heating rate produced by H_2 formation to the total rate of cooling (without H_2 formation heating) for each of the simulations. We use the rate coefficients k_4 ($\text{H} + \text{H} + \text{H} \rightarrow \text{H}_2 + \text{H}$) and k_6 ($\text{H} + \text{H} + \text{H}_2 \rightarrow \text{H}_2 + \text{H}_2$) from Palla et al. (1983) and assume an energy injection of 4.4 eV per reaction. We also include a cooling term representing the reverse of the above two reactions, using coefficients k_5 and k_7 of Palla et al. (1983). For metallicities $Z \leq 10^{-3.5} Z_\odot$, the ratio of the H_2 formation heating to the total cooling is 0.1 at $n \sim 10^9 \text{ cm}^{-3}$ and 1 at $n \sim 5 \times 10^9 \text{ cm}^{-3}$. For $Z = 10^{-3} Z_\odot$, this ratio is 0.1 at $n \sim 9 \times 10^7 \text{ cm}^{-3}$ and 1 at $n \sim 6 \times 10^8 \text{ cm}^{-3}$. For $Z \geq 10^{-2.5} Z_\odot$, this ratio is 0.1 at $n \sim 3 \times 10^7 \text{ cm}^{-3}$ and 1 at $n \sim 10^8 \text{ cm}^{-3}$. For run r3_Z-2noCMB, which has the CMB removed, this ratio is 0.1 at $n \sim 10^7 \text{ cm}^{-3}$ and 1 at $n \sim 10^8 \text{ cm}^{-3}$. For simulations with equivalent metallicities, the above ratio varies maximally by a factor of a few due to minor differences in the temperature at a given density. In all cases but one, fragmentation occurs well before H_2 formation heating becomes important. The lone exception is run r3_Z-3, where fragmentation occurs at $n \sim 3 \times 10^9 \text{ cm}^{-3}$ and H_2 formation heating matches the total cooling at $n \sim 10^9 \text{ cm}^{-3}$. However, the core in this simulation does not fragment until it has already begun to reheat due to adiabatic compression, so it is not clear what effect the inclusion of this missing heating term would have had.

In Figures 5 and 6, we plot the number density vs. gas temperature for the final output of each simulation. Due to the self-similar nature of the collapse, Figures 5 and 6 can also be used to understand the evolution of the central core throughout the collapse. In all the runs with $Z < Z_{cr}$, the cooling is too low to prevent the temperature from rising at the H_2 thermalization density, $n \sim 10^4 \text{ cm}^{-3}$. Therefore, the minimum fragmentation mass for these runs, set by the Jeans mass as the temperature minimum, is well over $1,000 M_\odot$, which is nearly equivalent to the total enclosed mass. Even though runs r1_Z-4 and r1_Z-3.75 are above Z_{cr} , the additional cooling provided by the metals is not sufficient to significantly lower the minimum fragmentation mass. For runs r1_Z-3.5 and r1_Z-3.25, the more efficient cooling lowers the minimum fragmentation mass to just over $100 M_\odot$, which is approximately a factor of a few lower than the total mass

within 1 pc.

For the runs with the highest metallicities, as in runs r1_Z-2.5 and r1_Z-2, the gas cools all the way to the temperature of the CMB. The cooling proceeds so efficiently that the gas has not had sufficient time to reach high densities before hitting the temperature floor of the CMB. Fragmentation can only continue as long as the temperature decreases with increasing density (Larson 1985, 2005). Although the temperature decreases slightly in runs r1_Z-2.5 and r1_Z-2 for densities greater than 10^3 cm^{-3} , the temperature minimum is effectively at $n = 10^3 \text{ cm}^{-3}$, where the gas reaches the CMB temperature. Near the CMB temperature, the value of the cooling rate, Λ , effectively becomes $(\Lambda(T) - \Lambda(T_{CMB}))$. Therefore, when the gas reaches the CMB temperature, the cooling rate drops to zero, and the cooling time becomes infinite. The gas cloud becomes extremely thermally stable, preventing further fragmentation.

To verify that the CMB is indeed suppressing fragmentation, we run one simulation, r3_Z-2_noCMB, with the CMB temperature floor removed. We choose initial conditions Set 3 for this exercise since it has the highest CMB temperature at the redshift of collapse and should therefore show the greatest contrast with the CMB removed. In Figure 7, we show mass-weighted mean number density projections of the central 5 pc for runs, r3_mf, r3_Z-2, and r3_Z-2_noCMB. Run r3_Z-2 has a much clumpier structure than its metal-free counterpart, even with the CMB temperature floor present. However, when the temperature floor is removed, the gas is able to collapse into a long, thin filament with far more small-scale structure. As shown in Figure 4, we find the most bound clumps in this run (4 within 1 pc of the density peak and 1 more within 5 pc). In Figure 8, we show mass-weighted mean temperature projections for the same runs as Figure 7. We overlay contours of projected mean number density of 10^4 cm^{-3} . Figure 6 shows that this is the approximate density at which the cloud in run r3_Z-2 first reaches the CMB temperature. In run r3_Z-2noCMB, it took $\sim 400,000$ years for the central density to increase from 10^4 cm^{-3} to 10^5 cm^{-3} , which is similar to the timescale in a dynamical collapse. In run r3_Z-2, the equivalent change in density took ~ 1.9 million years, indicating that cooling to the CMB temperature has indeed ended free-fall collapse.

In the projections of run r3_Z-2 in Figure 8, the 2 largest contours roughly represent the 2 bound clumps found within the 5 pc radius sphere. The gas within the clumps has a very uniform temperature, as its cooling has been abruptly halted at the CMB temperature ($\sim 71 \text{ K}$). The 2 clumps have masses of roughly 100 and 300 M_\odot . It is unlikely that they will fragment further, since the Jeans mass of each clump is nearly equivalent to its total mass. At a temperature of 71 K, sound waves will travel $\sim 1.7 \text{ pc}$ in the 1.9 Myr required for any additional fragments to increase in density by an order of magnitude once they have cooled to the CMB temperature. Any additional fragments that might possibly condense out of lower density gas must be approximately this large in order to collapse, suggesting they will also be very massive. It is interesting to note that the two bound clumps in the simulation are also about this size.

In contrast, the gas inside the contours of run r3_Z-2noCMB shows significantly more structure in tempera-

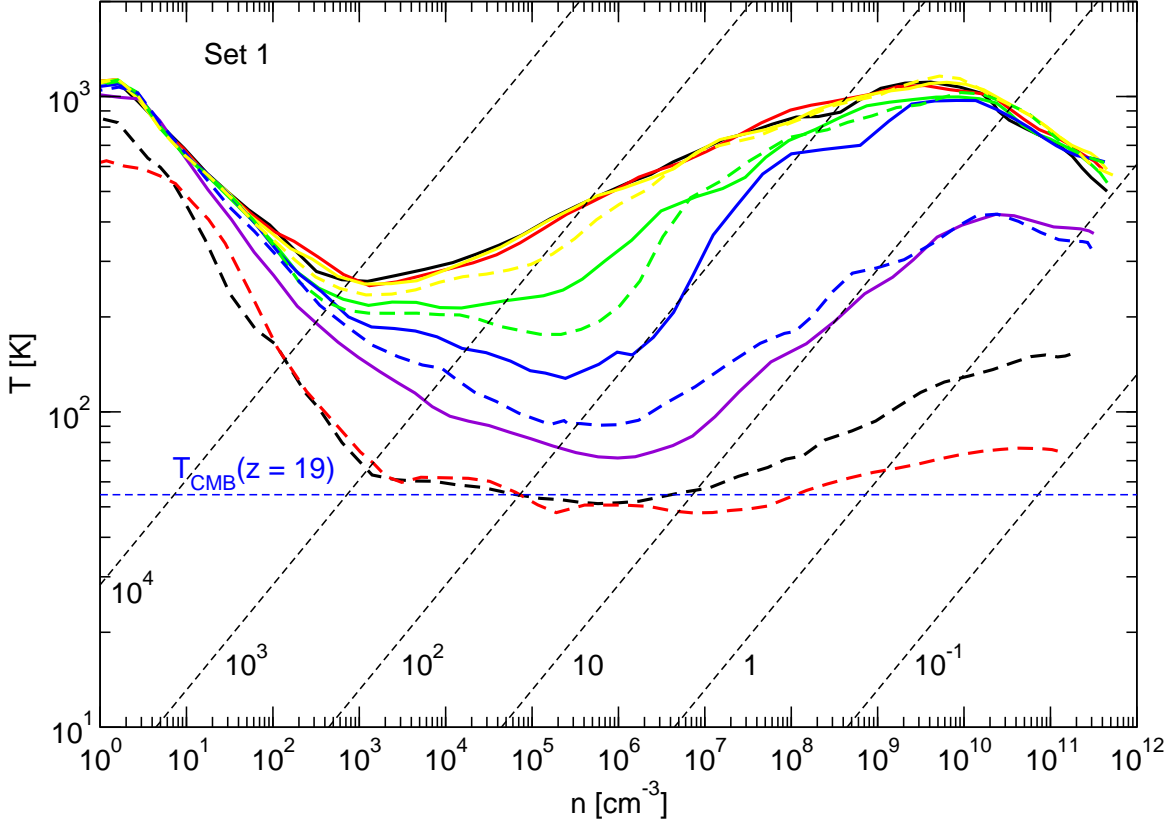


FIG. 5.— Mass-weighted, average temperature as a function of number density for all runs in Set 1. The colors are the same as in Figure 2, including the runs with metallicities $Z = 10^{-4.25}Z_{\odot}$ (dashed-yellow), $10^{-3.75}Z_{\odot}$ (dashed-green), and $10^{-3.25}Z_{\odot}$ (dashed-blue). The thin, black, dashed lines indicate lines of constant Jeans mass in M_{\odot} . The horizontal, blue, dashed line denotes the temperature of the CMB at $z = 19$, the approximate redshift of collapse for runs r1_Z-2.5 and r1_Z-2. The central cores in these two runs were both able to cool to the temperature of the CMB.

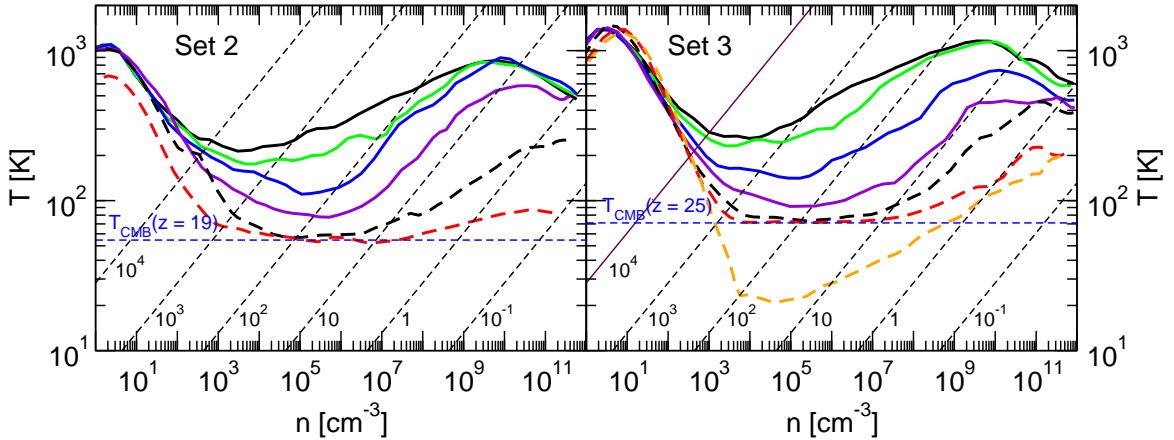


FIG. 6.— Mass-weighted, average temperature as a function of number density for all the runs in Set 2 (left) and Set 3 (right). For both panels, the metallicities are $Z = 0$ (solid-black), $10^{-4}Z_{\odot}$ (green), $10^{-3.5}Z_{\odot}$ (blue), $10^{-3}Z_{\odot}$ (purple), $10^{-2.5}Z_{\odot}$ (dashed-black), and $10^{-2}Z_{\odot}$ (dashed-red). In the bottom panel, the dashed-orange line corresponds to run r3_Z-2_noCMB, with $Z = 10^{-2}Z_{\odot}$, but with the CMB temperature floor removed. All curves in Figures 5 and 6 with the same colors refer to simulations with the same metallicities. The thin, black, dashed lines indicate lines of constant Jeans mass in M_{\odot} . The horizontal, blue, dashed lines denote the temperature of the CMB at $z = 19$ (left) and 25 (right).

ture. The cold knots in run r3_Z-2noCMB seen in Figure 8 correspond to the high density regions seen in Figure 7. 4 of the 5 bound clumps are Jeans unstable, with masses of 4, 4, 12, and $33 M_{\odot}$. The fifth, with $M \sim 0.5M_{\odot}$, is approximately 1/6 of its Jeans mass. The most massive clump is about 5 times more massive than its Jeans mass.

4. DISCUSSION

We have shown that fragmentation occurs within a collapsing cloud when the metallicity is above the critical metallicity. The exact value of the critical metallicity required to prevent an increase in temperature at the stalling point of H_2 varies slightly from halo to halo. Within our three sets of initial conditions, the values of Z_{cr} are correlated to the collapse redshift of the metal-free runs, with the highest Z_{cr} corresponding to the highest redshift. However, it is unclear whether this is significant. If the metallicity is only marginally higher than Z_{cr} , fragmentation is unlikely to occur, as the increase in temperature at the H_2 stalling point is only delayed momentarily. Thus, it is unlikely that a sharp transition in star formation mode occurs at just the moment when the critical metallicity is reached.

Fragmentation is suppressed when the metallicity is high enough such that the gas is able to cool to the temperature of the CMB when the central density is still relatively low. We confirm that the CMB is responsible for the observed suppression of fragmentation by running an identical simulation without the CMB. In this simulation where the CMB is absent, we find more bound clumps than in any other of the runs in this study. 2 bound clumps were found in run r3_Z-2, where the gas was able to cool to the CMB temperature. However, both of these clumps were quite massive ($M \gtrsim 100M_{\odot}$), and we showed in §3.4 that it is unlikely that they will fragment into smaller objects. We observe a small amount of variance in the metallicity range in which fragmentation occurs that does not appear to be related to the CMB. Just as the exact value of Z_{cr} seems to vary from halo to halo, we suspect that the range of metallicities where fragmentation occurs will also be influenced by the individual properties of a halo as well as its particular evolution.

The mass scale of collapsing clumps can be estimated from the Jeans mass at the end of the cooling phase. This implies the existence of three distinct metallicity regimes for star formation. In the first regime, $Z \lesssim Z_{cr}$, which we refer to as the ‘primordial’ mode, metals do not provide enough additional cooling to allow the gas temperature to continue to decrease monotonically with increasing density when the core reaches the H_2 thermalization density. In this case, the collapse proceeds in a similar way to the metal-free scenario, resulting in the formation of a single, massive object. There is also the potential for stars forming in this mode to be somewhat less massive than the very first stars. The fragmentation mass scale for extremely low metallicity gas ($Z \ll Z_{cr}$) may be lowered though compression by shocks from Pop III supernovae and enhanced cooling from HD in relic HII regions (Mackey et al. 2003; Johnson & Bromm 2006).

At the other extreme, we define Z_{CMB} as the metallicity at which the gas can cool to the CMB temperature. When $Z \gg Z_{CMB}$, the cloud-core will efficiently cool to

the temperature of the CMB when the central density is still relatively low. In this scenario, fragmentation is limited by cooling rapidly to the CMB temperature, as the mass scale is determined by the Jeans mass at the density when the core first reaches the CMB temperature. We refer to this as the CMB-regulated star formation mode, similar to Tumlinson (2007b). As fragmentation is severely limited in this mode, these stars will most likely be more massive on average than the characteristic mass of stars forming today.

Finally, our simulations have shown that there exists a special range in metallicity, $Z_{cr} \leq Z < Z_{CMB}$, where the core does not reheat at the metal-free stalling point, but also cannot cool all the way to the CMB temperature. The minimum temperature is set only by the balance of radiative cooling and adiabatic heating. The mass scale is not regulated externally by the CMB, but rather internally by the metallicity-dependent gas-cooling. Hence, we term this the metallicity-regulated star formation mode. This mode produces the lowest mass stars of the three modes mentioned.

The CMB-regulated star formation mode creates a means by which a higher number of massive stars are formed in very early universe, when the CMB temperature was much higher. As the universe evolves, the CMB temperature will slowly decrease, which will increase the metallicity required to reach the CMB temperature, referred to here as Z_{CMB} . The decrease in the CMB temperature also means that the fragmentation mass scale will be lower at the point where the gas reaches the temperature floor. Thus, the characteristic mass of stars produced by the CMB-regulated mode will slowly decrease with time. This behavior is in agreement with the model of an IMF that evolves with redshift formulated by Larson (1998). As the metallicity threshold for the CMB-regulated mode advances to higher metallicity, the range of operation of the metallicity-regulated mode will extend to take its place. We lack sufficient data in this study to predict the evolution of Z_{CMB} with redshift. However, in a paper to follow, we will map out the evolution of Z_{CMB} vs. z with additional simulations collapsing as much lower redshifts. Observations of nearby star-forming clouds show that the minimum achievable temperature in the local universe is roughly 10 K (e.g., Evans (1999)). This implied that the CMB-regulated star formation mode is in operation up to $z \sim 2.7$, at the absolute latest. A growing amount of evidence has been presented that the stellar IMF evolves with redshift (e.g., Fardal et al. (2007); Tumlinson (2007b); van Dokkum (2008); Davé (2008); Wilkins et al. (2008)). Interestingly, van Dokkum (2008), Davé (2008), and Wilkins et al. (2008) report evidence from high redshift that the IMF may deviate from the standard Salpeter IMF, favoring higher mass stars for $z \gtrsim 2 - 4$.

If dust is present in the very early universe, this would extend the range of the metallicity-regulated star formation mode to metallicities as low as $Z \sim 10^{-5.5}Z_{\odot}$ (Omukai et al. 2005; Schneider et al. 2006; Tsuribe & Omukai 2006; Clark et al. 2008). The existence of low mass, hyper metal poor stars, HE0107-5240 (Christlieb et al. 2002), and HE1327-2326 (Frebel et al. 2005), both with $[Fe/H] < -5$, may provide evidence of this. Both of these stars show extremely enhanced C and O abundances, which would make their effective metallic-

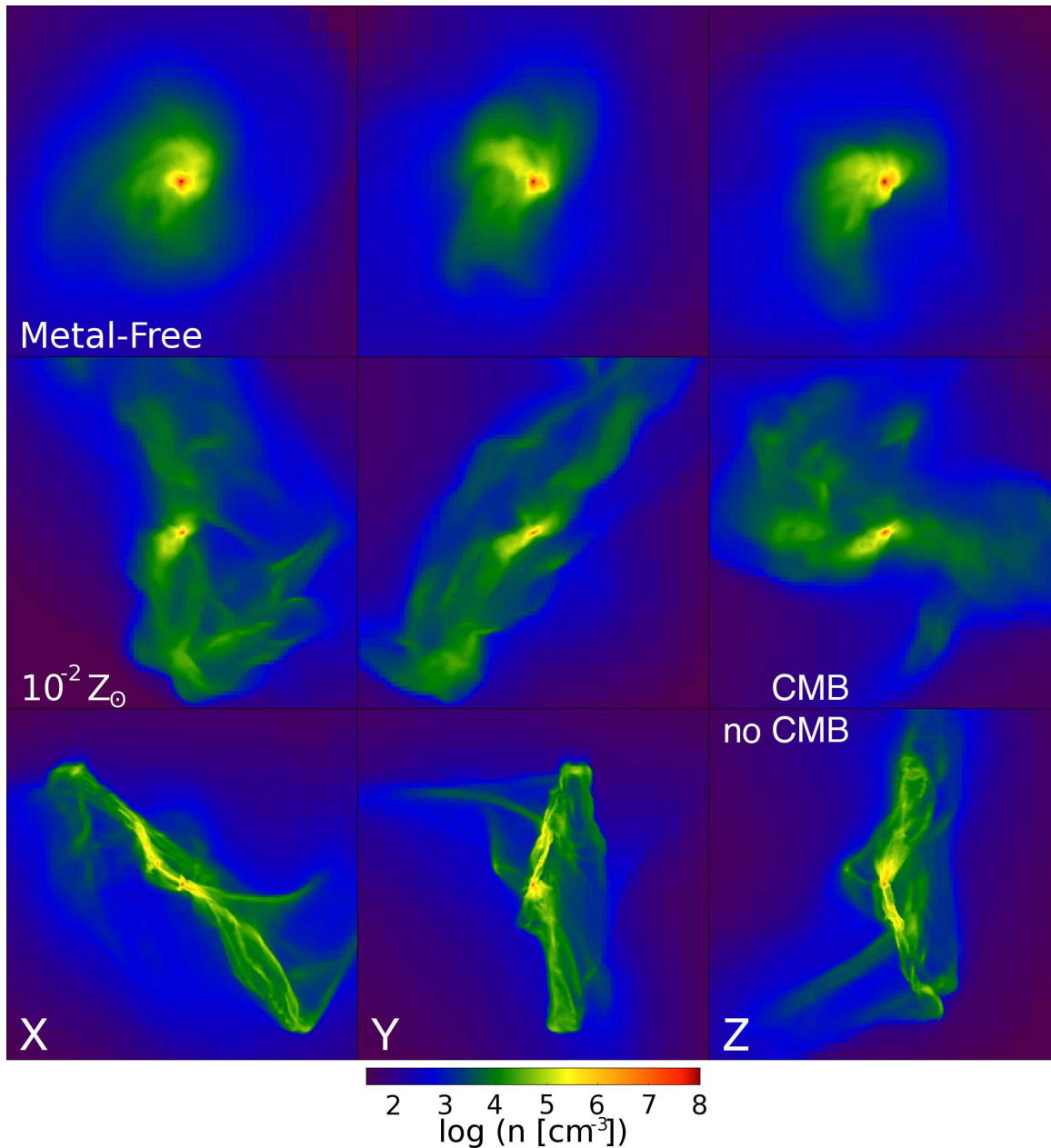


FIG. 7.— Projections of mass-weighted mean number density along the x (left), y (center), and z (right) axes for the final output of runs r3_mf with zero-metallicity (top), r3_Z-2 with $Z = 10^{-2} Z_{\odot}$ (middle), and r3_-2noCMB with $Z = 10^{-2} Z_{\odot}$ and the CMB temperature floor removed (bottom). Each projection is centered on the location of maximum density in the simulation box and has a width of 5 pc proper. The images were made with the YT analysis toolkit (Turk 2008, yt.enzotools.org).

ities (in terms of the radiative cooling ability of gas with that abundance) much higher. However, it is pointed out by Tumlinson (2007a,b), that the abundance patterns of these stars are best recreated by a scenario in which the C and O enhancement comes via binary mass transfer from an intermediate mass AGB star, meaning the stars are truly metal poor. In that case, these two low-mass stars would likely require dust in order to form at such low metallicity. Tumlinson (2007b) also shows that such a high fraction of carbon enhanced metal poor stars (CEMPs) requires a higher than normal fraction of more massive stars that go through the AGB phase. Tumlinson (2007b) claims that the evolution of CEMP fraction with metallicity (with a higher CEMP fraction at lower metallicity) already shows the influence of the CMB on the IMF. If a CEMP star and its binary compan-

ion were formed from gas at the same metallicity, there would have to be process at work that would prevent the dust cooling fragmentation from forming only low mass stars. The star formation models of Omukai et al. (2005) do not indicate that the dust cooling phase that induces low mass fragmentation is able to reach the CMB temperature for $Z < 10^{-4} Z_{\odot}$. This may simply imply that metal mixing from the first supernovae is highly heterogeneous, allowing stars to form simultaneously with largely different abundances.

In this work, we study only gas clouds with solar abundance patterns. Most likely, the first metals in the universe will not have solar abundance patterns. However, from the perspective of simulating metal-enriched star formation, it is not the specific elemental abundances of a gas cloud that are important, but rather the total cool-

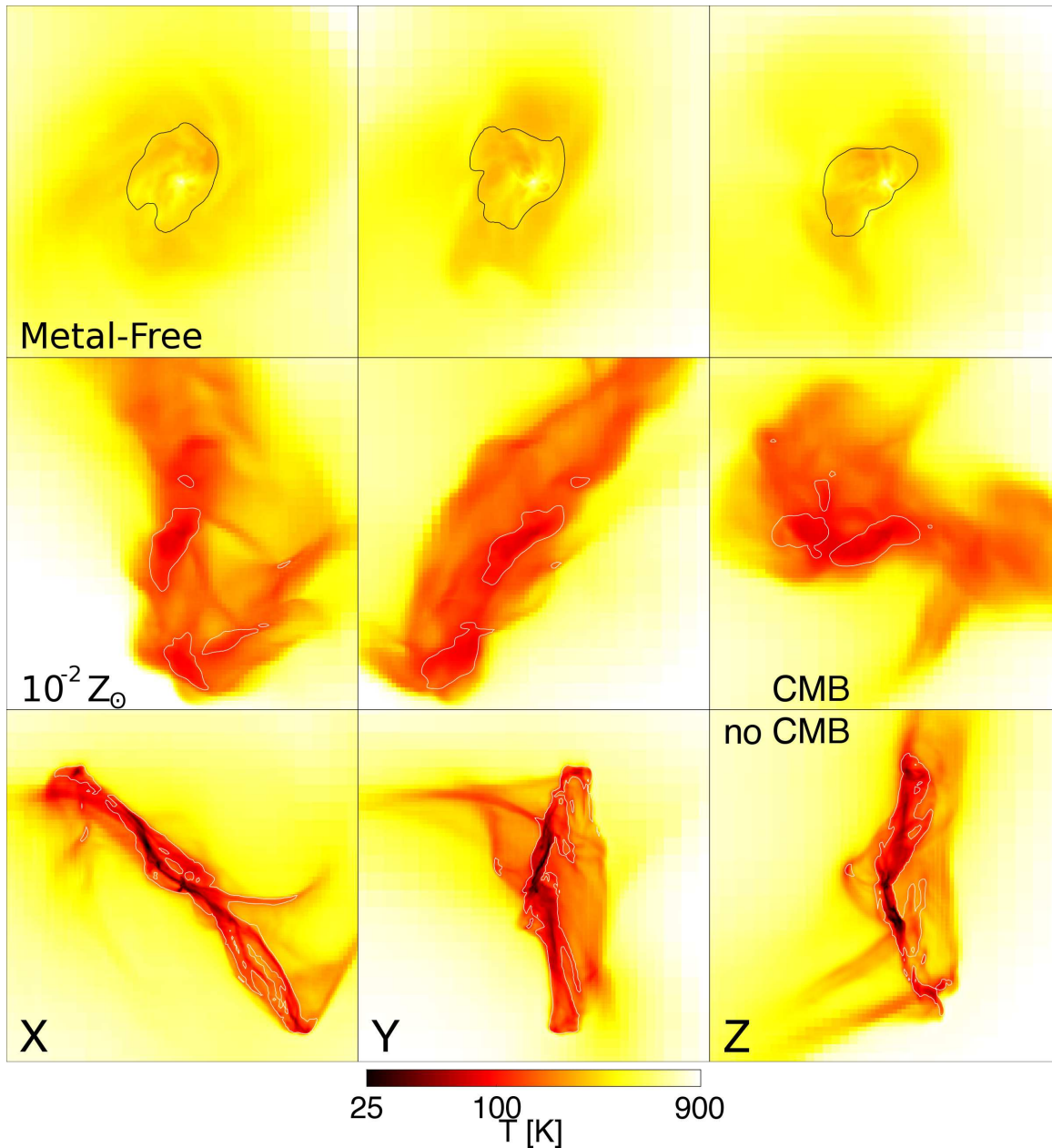


FIG. 8.— Projections of mass-weighted mean temperature density along the x (left), y (center), and z (right) axes for the final output of runs r3_mf with zero-metallicity (top), r3_Z-2 with $Z = 10^{-2}Z_{\odot}$ (middle), and r3_-2noCMB with $Z = 10^{-2}Z_{\odot}$ and the CMB temperature floor removed (bottom). Each projection is centered on the location of maximum density in the simulation box and has a width of 5 pc proper. The solid lines show contours of projected mean number density of 10^4 cm^{-3} . The images were made with the YT analysis toolkit (Turk 2008, yt.enzotools.org).

ing rate produced by the gas. Therefore, given that it is the sum of the metals that is important, and not the abundance pattern, the results of this work are robust in spite of the fact that the abundance patterns used are likely to be incorrect.

There appears to be some discrepancy between our results and those of Jappsen et al. (2007), who see no evidence of fragmentation induced by gas-phase metal cooling. This is potentially resolved by the fact that in that work, the gas collapse is only strictly followed up to densities of $5 \times 10^2 \text{ cm}^{-3}$ before sink particles are created. Figures 5 and 6 show very little difference in the thermal structure of the gas for densities below $5 \times 10^2 \text{ cm}^{-3}$. Additionally, our clump finding algorithm found only a single bound clump within every simulation when

the analysis was performed on data outputs that were made when the maximum density was only $\sim 10^3 \text{ cm}^{-3}$. Multiple clumps were only found when the clouds had reached somewhat higher densities. Finally, the simulations in this work began with cold, neutral gas, whereas their simulations began with hot, ionized gas. Had their simulations been run to higher densities, any dissimilarities might also be due to using different initial conditions.

5. CONCLUSION

We have performed a series of high resolution simulations of metal-enriched star formation using cosmological, Pop III style initial conditions, and assuming fully homogeneous metal enrichment. We have shown that our results apply to more than a single star forming region

by using 3 different sets of initial conditions with identical cosmological parameters and resolution, but with 3 unique random seeds with which to create the initial perturbations in the density and velocity fields. From the results of these simulations, the main conclusions of this work are:

1. Fragmentation does not occur when the metallicity is only slightly above Z_{cr} , since this only leads to a small delay in the onset of the loitering phase that is brought on by a decrease in the efficiency of H_2 cooling. The density at which the temperature begins to increase with increasing density is only marginally higher than in the metal-free case, and therefore does not lead to a significant lowering of the minimum Jeans mass. Within our simulations, Z_{cr} is roughly $10^{-3.9}Z_{\odot}$. We find that fragmentation does not occur until the metallicity is roughly 0.5 dex above Z_{cr} .

2. Fragmentation is suppressed when the metallicity is high enough such that the gas is able to cool to the temperature of the CMB when the density of the collapsing cloud is still relatively low ($n \sim 10^4 \text{ cm}^{-3}$). The Jeans mass at the density and temperature at which the cloud first reaches the CMB temperature sets the minimum fragmentation mass within the cloud, and as such only massive clumps are able to form.

3. Metal-enriched star formation occurs in three modes that are separated by two metallicity thresholds, Z_{cr} and Z_{CMB} . Z_{cr} is the conventional critical metallicity and Z_{CMB} is the metallicity at which the gas is able to cool to the temperature of the CMB at a given redshift. At the approximate collapse redshifts of our simulations, $z \sim 20$, Z_{CMB} is between 10^{-3} and $10^{-2.5}Z_{\odot}$. The three modes of star formation are:

- The primordial mode ($Z < Z_{cr}$) - The additional cooling provided by the metals is not enough to significantly alter the thermal structure of the cloud relative to the metal-free case. No fragmentation occurs and the star will have a mass similar to a Pop III star.
- The metallicity-regulated mode ($Z_{cr} < Z < Z_{CMB}$) - Metal cooling is high enough to allow the cloud to continue to cool past the metal-free loitering phase, but not high enough to cool it to the temperature of the CMB. The minimum fragmentation mass is set at lower temperatures and higher densities than in the primordial case and fragmentation into multiple objects occurs. Based on the masses of clumps formed within our simulations, stars forming in this mode could have masses of

the order of a few M_{\odot} or less.

- The CMB-regulated mode ($Z > Z_{CMB}$) - Fragmentation is suppressed when the cloud is able to cool to the CMB temperature, as is described in point 2 of the conclusions. At minimum, stars forming in the CMB-regulated mode will be more massive than stars forming in the metallicity-regulated mode. Z_{CMB} will increase as the CMB temperature lowers with time. As such, the masses of stars forming in the CMB-regulated mode will slowly decrease. This mode will vanish altogether when the CMB temperature reaches the observed minimum temperature of nearby molecular clouds ($T \sim 10 \text{ K}$ at $z \sim 2.7$).

4. By demonstrating that the CMB can suppress fragmentation, we have provided a key conceptual piece CMB-IMF hypothesis (Tumlinson 2007b). As pointed out by Tumlinson (2007b), an IMF that evolves with redshift, producing more massive stars in the past, has consequences that may already be testable by observations.

We are extremely grateful to an anonymous referee who provided comments that significantly strengthened the arguments presented and helped to improve the manuscript a great deal. BDS would like to thank Jason Tumlinson and Simon Glover for extremely insightful discussions, as well as Gary Ferland and Peter van Hoof for their assistance with the Cloudy code. BDS and SS thank the Aspen Center for Physics for their hospitality during the 2008 Aspen Winter Conference On Astrophysics. This work was made possible by Hubble Space Telescope Theory Grant HST-AR-10978.01. BWO and BDS carried out portions of this work under the auspices of the National Nuclear Security Administration of the U.S. Department of Energy at Los Alamos National Laboratory under Contract No. DE-AC52-06NA25396. BDS was supported at the University of Colorado, Boulder by NASA Theory grant NNX07AG77G. BWO was supported by a LANL Director’s Postdoctoral Fellowship (DOE LDRD grant 20051325PRD4). MJT performed this work under the auspices of the Department of Energy at the Stanford Linear Accelerator Center in the Kavli Institute for Particle Astrophysics and Cosmology under Contract No. DE-AC02-76SF00515. The simulations were performed at SDSC with computing time provided by NRAC allocations MCA98N020 and TG-AST070010N.

REFERENCES

- Abel, T., Anninos, P., Zhang, Y., & Norman, M. L. 1997, *New Astronomy*, 2, 181
- Abel, T., Bryan, G. L., & Norman, M. L. 2002, *Science*, 295, 93
- Anninos, P., Zhang, Y., Abel, T., & Norman, M. L. 1997, *New Astronomy*, 2, 209
- Bromm, V., Coppi, P. S., & Larson, R. B. 2002, *ApJ*, 564, 23
- Bromm, V., Ferrara, A., Coppi, P. S., & Larson, R. B. 2001, *MNRAS*, 328, 969
- Bromm, V. & Loeb, A. 2003, *Nature*, 425, 812
- . 2004, *New Astronomy*, 9, 353
- Bryan, G. & Norman, M. L. 1997, in *Workshop on Structured Adaptive Mech Refinement Grid Methods*, ed. N. Chrisochoides, IMA Volumes in Mathematics No. 117 (Springer-Verlag)
- Christlieb, N., Bessell, M. S., Beers, T. C., Gustafsson, B., Korn, A., Barklem, P. S., Karlsson, T., Mizuno-Wiedner, M., & Rossi, S. 2002, *Nature*, 419, 904
- Clark, P. C., Glover, S. C. O., & Klessen, R. S. 2008, *ApJ*, 672, 757
- Davé, R. 2008, *MNRAS*, 385, 147
- Eisenstein, D. J. & Hu, W. 1999, *ApJ*, 511, 5
- Evans, II, N. J. 1999, *ARA&A*, 37, 311
- Fardal, M. A., Katz, N., Weinberg, D. H., & Davé, R. 2007, *MNRAS*, 379, 985
- Ferland, G. J., Korista, K. T., Verner, D. A., Ferguson, J. W., Kingdon, J. B., & Verner, E. M. 1998, *PASP*, 110, 761
- Field, G. B. 1965, *ApJ*, 142, 531

- Frebel, A., Aoki, W., Christlieb, N., Ando, H., Asplund, M., Barklem, P. S., Beers, T. C., Eriksson, K., Fechner, C., Fujimoto, M. Y., Honda, S., Kajino, T., Minezaki, T., Nomoto, K., Norris, J. E., Ryan, S. G., Takada-Hidai, M., Tsangarides, S., & Yoshii, Y. 2005, *Nature*, 434, 871
- Galli, D. & Palla, F. 1998, *A&A*, 335, 403
- Gao, L., Yoshida, N., Abel, T., Frenk, C. S., Jenkins, A., & Springel, V. 2007, *MNRAS*, 378, 449
- Glover, S. 2008, in *American Institute of Physics Conference Series*, Vol. 990, *First Stars III*, ed. B. W. O'Shea & A. Heger, 25–29
- Green, D. A., Tuffs, R. J., & Popescu, C. C. 2004, *MNRAS*, 355, 1315
- Greif, T. H., Johnson, J. L., Bromm, V., & Klessen, R. S. 2007, *ApJ*, 670, 1
- Heger, A. & Woosley, S. E. 2002, *ApJ*, 567, 532
- Jappsen, A.-K., Glover, S. C. O., Klessen, R. S., & Mac Low, M.-M. 2007, *ApJ*, 660, 1332
- Johnson, J. L. & Bromm, V. 2006, *MNRAS*, 366, 247
- Kitayama, T. & Yoshida, N. 2005, *ApJ*, 630, 675
- Komatsu, E., Dunkley, J., Nolta, M. R., Bennett, C. L., Gold, B., Hinshaw, G., Jarosik, N., Larson, D., Limon, M., Page, L., Spergel, D. N., Halpern, M., Hill, R. S., Kogut, A., Meyer, S. S., Tucker, G. S., Weiland, J. L., Wollack, E., & Wright, E. L. 2008, *ArXiv e-prints*, 803
- Krause, O., Birkmann, S. M., Rieke, G. H., Lemke, D., Klaas, U., Hines, D. C., & Gordon, K. D. 2004, *Nature*, 432, 596
- Larson, R. B. 1985, *MNRAS*, 214, 379
- . 1998, *MNRAS*, 301, 569
- . 2005, *MNRAS*, 359, 211
- . 2007, *ArXiv Astrophysics e-prints*
- Lepp, S. & Shull, J. M. 1984, *ApJ*, 280, 465
- Mackey, J., Bromm, V., & Hernquist, L. 2003, *ApJ*, 586, 1
- Maeder, A., Meynet, G., & Hirschi, R. 2005, in *Astronomical Society of the Pacific Conference Series*, Vol. 336, *Cosmic Abundances as Records of Stellar Evolution and Nucleosynthesis*, ed. T. G. Barnes, III & F. N. Bash, 79–+
- Nomoto, K., Tominaga, N., Umeda, H., Kobayashi, C., & Maeda, K. 2006, *Nuclear Physics A*, 777, 424
- Omukai, K. 2000, *ApJ*, 534, 809
- Omukai, K. & Palla, F. 2003, *ApJ*, 589, 677
- Omukai, K., Tsuribe, T., Schneider, R., & Ferrara, A. 2005, *ApJ*, 626, 627
- O'Shea, B. W., Bryan, G., Bordner, J., Norman, M. L., Abel, T., Harknes, R., & Kritsuk, A. 2004, in *Lecture Notes in Computational Science and Engineering*, Vol. 41, *Adaptive Mesh Refinement - Theory and Applications*, ed. T. Plewa, T. Linde, & V. G. Weirs
- O'Shea, B. W. & Norman, M. L. 2007, *ApJ*, 654, 66
- Palla, F., Salpeter, E. E., & Stahler, S. W. 1983, *ApJ*, 271, 632
- Rockefeller, G., Fryer, C. L., & Li, H. 2006, *ArXiv Astrophysics e-prints*
- Santoro, F. & Shull, J. M. 2006, *ApJ*, 643, 26
- Schneider, R., Ferrara, A., & Salvaterra, R. 2004, *MNRAS*, 351, 1379
- Schneider, R., Ferrara, A., Salvaterra, R., Omukai, K., & Bromm, V. 2003, *Nature*, 422, 869
- Schneider, R., Omukai, K., Inoue, A. K., & Ferrara, A. 2006, *MNRAS*, 369, 1437
- Shu, F. H. 1977, *ApJ*, 214, 488
- Smith, B., Sigurdsson, S., & Abel, T. 2008, *MNRAS*, 385, 1443
- Smith, B. D. & Sigurdsson, S. 2007, *ApJ*, 661, L5
- Smith, M. S., Kawano, L. H., & Malaney, R. A. 1993, *ApJS*, 85, 219
- Spergel, D. N., Bean, R., Doré, O., Nolta, M. R., Bennett, C. L., Dunkley, J., Hinshaw, G., Jarosik, N., Komatsu, E., Page, L., Peiris, H. V., Verde, L., Halpern, M., Hill, R. S., Kogut, A., Limon, M., Meyer, S. S., Odegard, N., Tucker, G. S., Weiland, J. L., Wollack, E., & Wright, E. L. 2007, *ApJS*, 170, 377
- Tan, J. C. & McKee, C. F. 2004, *ApJ*, 603, 383
- Truelove, J. K., Klein, R. I., McKee, C. F., Holliman, II, J. H., Howell, L. H., & Greenough, J. A. 1997, *ApJ*, 489, L179+
- Truelove, J. K., Klein, R. I., McKee, C. F., Holliman, II, J. H., Howell, L. H., Greenough, J. A., & Woods, D. T. 1998, *ApJ*, 495, 821
- Tsuribe, T. & Omukai, K. 2006, *ApJ*, 642, L61
- Tumlinson, J. 2007a, *ApJ*, 665, 1361
- . 2007b, *ApJ*, 664, L63
- Turk, M. 2008, in *Proceedings of the 7th Python in Science Conference*, ed. G. Varoquaux, T. Vaught, & J. Millman, Pasadena, CA USA, 46 – 50
- van Dokkum, P. G. 2008, *ApJ*, 674, 29
- Wilkins, S. M., Trentham, N., & Hopkins, A. M. 2008, *MNRAS*, 385, 687
- Yoshida, N., Omukai, K., Hernquist, L., & Abel, T. 2006, *ApJ*, 652, 6